

Epidemic spreading and herd immunity in a driven non-equilibrium system of strongly-interacting atoms

Dong-Sheng Ding,^{1,2,*} Zong-Kai Liu,^{1,2} Hannes Busche,³ Bao-Sen Shi,^{1,2,†} Guang-Can Guo,^{1,2} Charles S. Adams,^{4,‡} and Franco Nori^{5,6,7,§}

¹*Key Laboratory of Quantum Information, University of Science and Technology of China, Hefei, Anhui 230026, China.*

²*Synergetic Innovation Center of Quantum Information and Quantum Physics, University of Science and Technology of China, Hefei, Anhui 230026, China.*

³*Department of Physics, Chemistry and Pharmacy, Physics@SDU, University of Southern Denmark, 5230 Odense M, Denmark*

⁴*Department of Physics, Joint Quantum Centre (JQC) Durham-Newcastle, Durham University, South Road, Durham DH1 3LE, United Kingdom.*

⁵*Theoretical Quantum Physics Laboratory, RIKEN Cluster for Pioneering Research, Wako-shi, Saitama 351-0198, Japan.*

⁶*RIKEN Center for Quantum Computing (RQC), Wako-shi, Saitama 351-0198, Japan.*

⁷*Physics Department, The University of Michigan, Ann Arbor, MI 48109-1040, USA.*

(Dated: June 24, 2021)

It is increasingly important to understand the spatial dynamics of epidemics. While there are numerous mathematical models of epidemics, there is a scarcity of physical systems with sufficiently well-controlled parameters to allow quantitative model testing. It is also challenging to replicate the macro non-equilibrium effects of complex models in microscopic systems. In this work, we demonstrate experimentally a physics analog of epidemic spreading using optically-driven non-equilibrium phase transitions in strongly interacting Rydberg atoms. Using multiple laser beams we can impose any desired spatial structure. We observe spatially localized phase transitions and their interplay in different parts of the sample. These phase transitions simulate the outbreak of an infectious disease in multiple locations, as well as the dynamics towards “herd immunity” and “endemic state” in different regimes. The reported results indicate that Rydberg systems are versatile enough to model complex spatial-temporal dynamics.

Self-organization and non-equilibrium dynamics of complex systems emerge not only in physics, but also in other fields such as earth science, biology, and economics [1]. In these cases, many interacting degrees of freedom are repelling, such as sand and rice grains [2], vortices [3, 4], etc. and they can be temporally stuck in metastable states, due to local traps or due to static friction. When slowly driven towards marginal stability, these extended systems exhibit avalanches at various length scales [2–4]. Rydberg atoms allow to model spatial dynamics with emerging complexity [5–9]. These atoms combine the precision of atomic physics with strong interactions with neighboring atoms, more common in condensed matter systems [10, 11]. Rydberg atoms are not only ideal for applications in quantum technology and computing [12–14], but also as a potential model

system for simulations [14–16]. Precise control of the excitation probability using narrowband lasers [17, 18] makes Rydberg atoms an excellent candidate to study non-equilibrium physics, as instabilities of equilibrium states are ubiquitous processes occurring in a variety of driven Rydberg systems. For example, Rydberg atoms in different driven configurations exhibit many fascinating characteristics of complex systems, including aggregate formation [19], non-equilibrium phase transitions [20, 21], critical points [22], self-organized criticality [23, 24], epidemic growth [25], and hydrodynamics [26].

There is considerable interest in simulating the outbreak of infectious diseases. The accuracy of epidemic models has been considerably improved over time [27, 28]. It is desirable to study and replicate the macro non-equilibrium effects of complex dynamics in well-controlled microscopic atomic systems. Moreover, many non-equilibrium phenomena cannot be broken down to just two global stable states; and numerous real systems are spatially inhomogeneous, e.g. the outbreak of an infectious disease can occur in multiple locations [29]. The added interplay between multiple spatial domains results in additional complexity that manifests as both local and non-local dynamics. Consequently, the study of phase transitions in engineered spatially inhomogeneous systems is an important tool to improve our understanding of non-equilibrium dynamics in extended systems.

Here we model epidemic spreading dynamics using a laser-driven thermal Rydberg gas. We have observed the analog of typical transmission profiles for susceptible infected-susceptible (SIS) and susceptible-infected-recovered (SIR) processes. The intensity pattern of the laser beams creates a spatially inhomogeneous Rydberg excitation rate, and thus spatial domains with different Rydberg atom densities. Within each domain, the system can be found in one of two phases. Below a critical threshold density, interactions between Rydberg

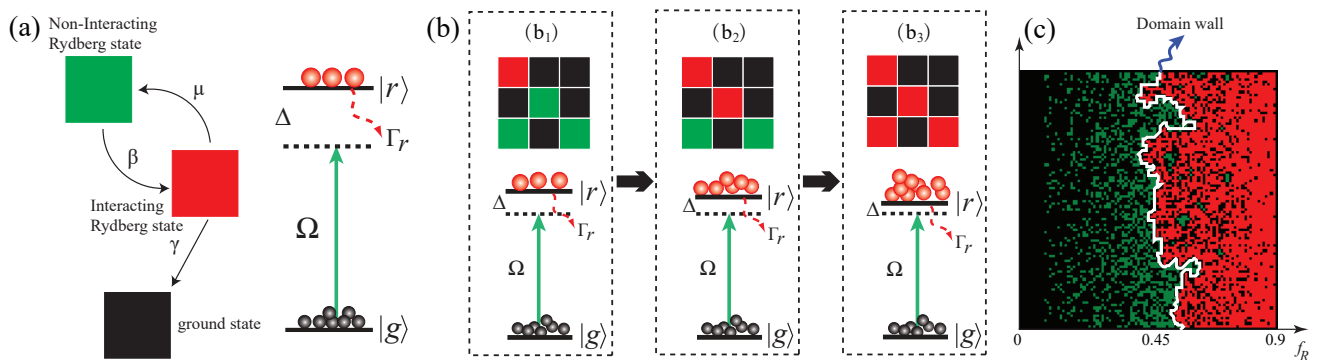


Figure 1. **Epidemic model simulation with Rydberg avalanche excitations.** (a) The model consists of three states: the interacting Rydberg state (red), the non-interacting Rydberg state (green) and the ground state (black). The right diagram shows the energy levels of atoms under a laser drive. Here, Δ is defined as the effective detuning between the Rydberg state $|r\rangle$ and the laser, and Γ_r is the decay rate of $|r\rangle$. (b) The algorithm of our 2D cellular automaton. The rule of updating cells in the susceptible-infected-recovered model is shown in (b₁–b₃): the cells are updated in the next step according to its current state and the state of its eight nearest neighbors. The susceptible infected-susceptible model satisfies the condition $\beta \gg \gamma$, $\gamma \rightarrow 0, \mu = 0.01$; while the susceptible-infected-recovered process obeys $\beta/\gamma > 1$ and $\mu \rightarrow 0$. The interacting Rydberg atoms spread out in the entire interacting region because the population-dependent energy shift Δ_{shift} induces a nonlinear ‘facilitated’ excitation, in which the effective detuning Δ between the laser and the Rydberg energy level of the excited state $|r\rangle$ is shifted. (c) A 2D snapshot of interacting Rydberg atoms (red) spreading in a $N = 100 \times 100$ inhomogeneous Rydberg density system (with fractions $f_R = 0\text{--}0.9$) after $i = 200$ iterations. There is an isolated boundary of contagion (marked in white), a domain wall separating the inhomogeneous distributions of Rydberg density.

atoms are negligible; We refer to this as the ‘non-interacting’ NI phase. Above the threshold, interactions between Rydberg atoms induce a shift and broadening of the Rydberg lines that facilitate Rydberg excitation in adjacent regions; This triggers a localized excitation avalanche and transitions to a ‘strongly-interacting’ I phase. We observe separate phase jumps and hysteresis loops associated with different spatial domains within our medium. The multiple hysteresis loops combine to produce multistability in the optical transmission. The experimental atomic system shows an initial exponential spread of the (microscopic) “epidemic”, until the system reaches two cases: one is “herd immunity”, which stops the spread in the SIR process; another is “endemic state”, which is a stationary state in the SIS case.

In order to gain insight into the spatial dynamics of Rydberg non-equilibrium phase transitions and, in particular, the spreading of the interacting phase, we build an avalanche model via the SIS and SIR models introduced in Refs. [29]. The elements of the effective model are schematically shown in Fig. 1(a); where β is the spreading rate from the non-interacting Rydberg state to the interacting Rydberg state, μ is the rate of the reverse process, and γ is the decay rate of the interacting Rydberg state to the ground state. The spreading process is simulated by a cellular automaton with the rules shown in Fig. 1(b). The model uses $N = m \times m$ 2D cells. Each cell updates according to its current state and the state of its eight nearest neighbors. First, the cells are randomly filled with fractions f_R of Rydberg atoms. A cell is in the NI phase if $f_R < f_{R,c}$ [green cells in Fig. 1(b)], in the

I phase if $f_R > f_{R,c}$ (red), or in a depleted phase (black) without Rydberg atoms in the cell. These situations correspond to a susceptible person, an infected person, or an immune site, in the original epidemic model [29].

The procedure schematically shown in Fig. 1(b) describes the following steps: if the fraction f_R of Rydberg atoms in an arbitrary cell [red cells in figure 1(b₁)] exceeds the critical fraction $f_{R,c}$, and is thus in the interacting phase, it increases the excitation probability of neighboring Rydberg atoms [green cells in Fig. 1(b₁)] f_R to be above $f_{R,c}$, such that the neighboring cells transition to the interacting phase as well in the next iteration [red cells in Fig. 1(b₂)]. This occurs due to level shifts Δ_{shift} by strong interactions that result in a ‘facilitated’ excitation process, which triggers an avalanche process throughout the interaction region, corresponding to the epidemic spreading to adjacent sites; see the energy diagrams in Fig. 1(b₁–b₃). We consider the condition $\beta \gg \gamma, \mu$ for the following SIS simulation, which corresponds to fast scanning either the probe intensity or Δ_c , and the system changes from the NI to the I phase. Otherwise, the system would oscillate near the critical point, and the oscillations between the phases display a bimodal distribution of transmission levels as demonstrated in Ref. [24], see also [30]. The boundary condition in our model is such that interacting Rydberg atoms at the edges disappear as they would move out of the excitation volume defined by the laser beams.

We have simulated the dynamics of ‘facilitated’ Rydberg excitations according to the cellular automaton,

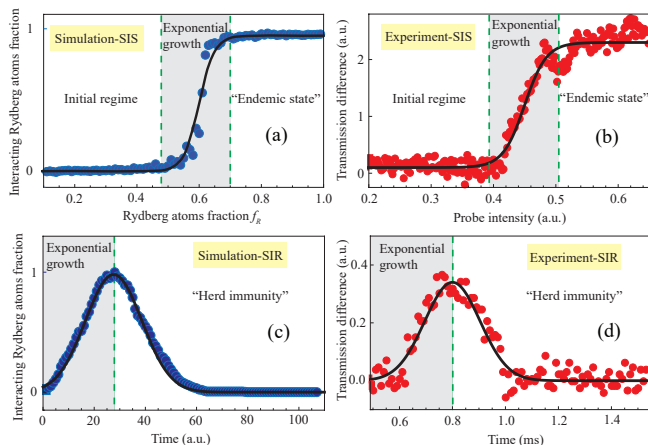


Figure 2. **Epidemic nonlinear spreading** (a) SIS model by simulating avalanche behavior of interacting Rydberg atoms via a cellular automaton in an $N = 100 \times 100$ cells system. (b) Measured phase transition versus probe intensity. The solid lines in (a) and (b) are fit by the hyperbolic tangent function $A + B \tanh[(x - C)/\omega]$, with parameters $A = B = 0.47$, $C = 0.6$ and $\omega = 0.05$ for (a), and $A = 0.12$, $B = 0.11$, $C = 0.45$ and $\omega = 0.035$ for (b). (c) SIR model showing a peak versus time. (d) The measured transmission in time without scanning laser detuning. The solid lines in (c) and (d) are fit by the Gaussian function $Be^{-\omega(t-C)^2}$ with parameters $B = 0.98$, $C = 27.6$ and $\omega = 0.0041$ for (c), and $B = 0.034$, $C = 0.8$ and $\omega = 46$ for (b). The dynamics is divided in three regimes: initial, exponential growth, and “herd immunity” or “endemic state”. The gray areas in (a-d) are the exponential growth regions (or nonlinear outbreak) in the epidemic process.

see Fig. 1(c). After $i = 200$ iterations in a 2D inhomogeneous Rydberg density system from fractions $f_R = 0$ to $f_R = 0.9$, respectively, with $m = 100$, there is an isolated boundary edge [shown in white in Fig. 1(c)] or “domain wall” that splits up the NI and I phases. On the contrary, there are no obvious domain walls if using a uniform atomic density. In the latter case, we record the Rydberg atoms density in the I phase after 200 iterations, and the simulated result is shown in Fig. 2(a). The interacting Rydberg fraction versus the Rydberg density f_R shows a critical point near a Rydberg fraction $f_{R,c} = 0.55-0.65$. In the experiment, we measure the transmission of the probe beam against the Rydberg atoms fraction by increasing the probe intensity in a two-photon electromagnetically induced transparency (EIT) scheme, see more details on the experimental configuration in [30]. There is a sudden jump in the probe transmission spectrum given in Fig. 2(b), which corresponds to the system transition from the NI to the I phase within the exponential growth regime. The threshold effect in the spreading of the interacting Rydberg atoms is consistent with the nonlinear spreading characteristics in the SIS model, as predicted in Fig. 2(a). In the case, the system is

scanned in a fast rate (see more details in [30]), the NI and I phases tends to dynamical equilibrium, which predicts a stationary “endemic state”, a main character of SIS model. When we consider the SIR process, the parameters β and μ satisfy $\beta/\gamma > 1$ and $\mu \rightarrow 0$, corresponding to the case of measuring the Rydberg excitations without scanning the laser detuning in the experiment. We have simulated the results in Fig. 2(c) with $\beta = 0.95$ and $\gamma = 0.2$. The interacting Rydberg atoms fraction first increases due to the contagion effect in the exponential regime, and then suddenly decreases because the system reaches “herd immunity” via the “infection recovery channel” in the SIR process. We have also measured the probe transmission spike near the critical point in the time domain, as shown in Fig. 2(d). The experimental Rydberg system shows the exponential spread of the (microscopic) epidemic until it reaches “herd immunity”.

The nonlinear spreading of the I phase is strongly dependent on the initial Rydberg density $f_R(t=0)$. This reveals that one uniform spatial domain leads to one jump, and multiple spatial domains lead to multiple jumps. This corresponds to the scenario of an outbreak of an infectious disease in different locations. In the experiment, a spatial inhomogeneity is introduced by subjecting part of the atomic vapor to localized perturbing beams. The additional perturbing fields have the same frequency as the optical probe field, but intersect the latter at an angle, creating regions with different intensities, as explained in [30]. Note

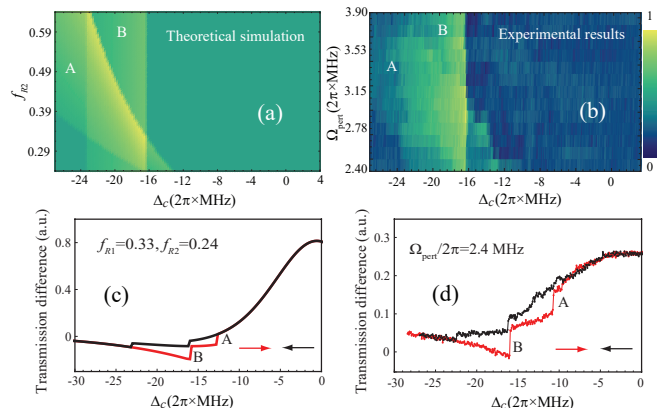


Figure 3. **Multi-domain bistability.** Comparison of the (a) theoretically, and (b) experimentally observed probe transmission. The probe transmission versus the coupling detuning Δ_c are shown in (c) theory and (d) experiments. The two Rydberg fractions f_{R1} and f_{R2} are fixed in (c) and the perturbing field Rabi frequency Ω_{pert} is fixed in (d). The areas indicated by A and B show their individual bistability regions, which add up to multi-stability where they overlap. The hysteresis loops of multistability are shown in (c) theory and (d) experiment. Positive (+) and negative (-) scan directions are shown in red and black, respectively.

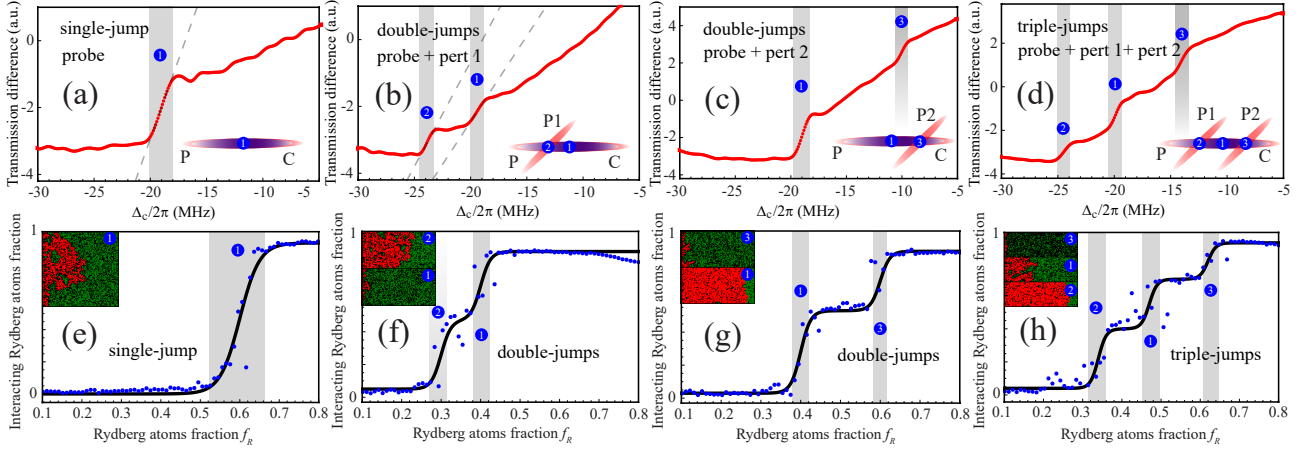


Figure 4. **Multiple phase jumps.** Panels (a)-(d) show, respectively, spectra with single-, double- and triple-jumps in the transmission. The different spectra are obtained by adding the additional perturbing fields 1 and 2 to create two and three domains. In these cases, the angles between the probe and the two perturbing fields are 7° and 14° , respectively. The dashed lines given in (a) and (b) are the slopes of the jumps. Here, $\Omega_{\text{pert},1} = 2\pi \times 3.7$ MHz and $\Omega_{\text{pert},2} = 2\pi \times 2.2$ MHz. Panels (e)-(h) show our simulations using the SIS cellular automaton [24, 31] with one, two, and three spatial domains, respectively. The solid lines in these simulations are fit by the function $A + \sum B_i \tanh((x - C_i)/\omega_i)$ including a series of tanh steps with different position C_i and width ω_i . We initialize the domain with atomic fractions $f_{R1} = f_R$ in (e) and $f_{R1} = f_R + 0.2$, $f_{R2} = f_R + 0.3$ in (f), $f_{R1} = f_R + 0.2$ and $f_{R3} = f_R$ in (g) and $f_{R2} = f_R + 0.3$, $f_{R1} = f_R + 0.15$, $f_{R3} = f_R$ in (h). The insets show the spread of interacting atoms (red) from left to right following 100 iterations.

that, a domain boundary can also arise from the attenuation of the probe light along with the medium [20]. For any spatially varying intensity distribution, the distinct phases are characterized by a spatial boundary between the states of high and low population. The occurrence of optical multistability and non-equilibrium phase transitions in a multi-domain system can be simulated using an EIT master equation with a mean-field model, see [30]. The multiple discrete transmission levels arise as the transition threshold is reached for different detunings in each domain.

In order to simulate the non-equilibrium behavior of the spatial domains in our phenomenological model, we consider distinct fractions f_{R1} and f_{R2} to each domain and their overall optical response. We then plot a color map of the transmission difference for the $+/-$ scan directions against f_{R2} and Δ_c by setting $f_{r1} = 0.33$, as in Fig. 3(a). For the experiments, we extract the transmission difference for the $+/-$ scan directions and plot the probe transmission versus Ω_{pert} and Δ_c in Fig. 3(b). In both theory and experiments, we observe two bistable regimes, and a multistable regime with overlapping regions. We also plot the transmission for the $+/-$ scan directions for theory and experiments, as shown in Figs. 3(c) and (d). The optical responses for multiple spatial domains show a double optical bistability, as described in [30].

It is insightful to increase the number of spatial domains in the experiments, and hence the number of phase jumps, by adding a few perturbing laser beams. Figures 4(a-d) show the transmission spectra with 1, 2,

and 3 discrete jumps, obtained by scanning Δ_c from red- to blue-detuning. Figure 4(a) refers to the single domain created by the probe field, showing a sudden jump in the transmission of light [gray region (1), where $\Delta_c/2\pi \sim -19$ MHz]. As we add the perturbing field 1 overlapping with the probe, the jump in Fig. 4(a) is split into two jumps in Fig. 4(b), these located at the detuning $\Delta_c/2\pi \sim -19$ MHz and $\Delta_c/2\pi \sim -24$ MHz, respectively. The three jumps in Fig. 4(d) correspond to three regions of higher Rydberg density associated with the probe and the perturbing fields 1 and 2. This added interplay between multiple spatial domains results in additional complexity that manifests in the additional jumps in Fig. 4(b). Meanwhile, the phase transition is weakened, as seen from the decreased height of each jump and the susceptibility of the phase transition defined as $dT/d\Delta_c$ (dT is the transmission difference of the jump) is reduced near the transition point $\Delta_c/2\pi \sim -19$ MHz. Figure 4(c) shows the corresponding situation when applying a perturbing field 2. In these two cases, as Δ_c approaches resonance, f_R increases and eventually one domain reaches the threshold $f_R^{(1)}$ at position 1 and another domain reaches the threshold $f_R^{(2)}$, the system undergoes two non-equilibrium phase transitions accompanied by two sudden jumps in the optical transmission. Figure 4(d) shows three jumps created by both the probe and perturbing fields 1 and 2. Changing the alignment determines whether these regions overlap or are separate. Here, we extend the epidemic model to multiple spatial domains according

to the 2D SIS cellular automaton. The qualitative agreement between the predicted phase jumps, Figs. 4(e-h), and the experimental observations, Figs. 4(a-d), confirms that we can associate each jump with an individual domain.

Non-equilibrium phase transitions within multi-domains often correspond to optical multistability, as demonstrated here, which is the extension of optical bistability to three or more stable output states. Before this work, multistability has been predicted and investigated in coupled atom-cavity systems [32–35] and semiconductor microcavities [36–40]. Optical bistability in Rydberg atoms has previously been studied both in theory [22, 41–44] and experiments [20, 21, 24, 45, 46]. However, optical multistability in Rydberg atoms is more challenging, and has not been explored before. A mean-field master Bloch equation can be used to qualitatively simulate multistability, because the individual Rydberg atoms interact with each other at random, in such a way that each Rydberg atom in a compartment is treated similarly and indistinguishably. More precise simulations in large-scale networks must consider the subtle differences between various states of the Rydberg atoms.

In summary, we have studied optically-driven multi-domain non-equilibrium dynamics in strongly interacting Rydberg atom gases. The measured hysteresis and phase jumps can be understood well and reproduced qualitatively using the epidemic model and using a mean-field master equation. Our results highlight the rich range of non-equilibrium phenomena that are accessible even in a relatively simple experiment and provide observational data to benchmark theoretical models of non-equilibrium dynamics under arbitrary spatial structures. Specifically, the observed dynamics of Rydberg atoms in different time and space scales could predict “herd immunity”, “endemic state” and the outbreak of a disease in multiple location. The reported multi-domain dependent exotic phases could help build a Rydberg-based simulate platform for more complex phenomena in real-world, such as in epidemiology [29], ecosystems and climate [1] or other complex systems [14].

We thank for Christopher G. Wade, Kevin J. Weatherill and Igor Lesanovsky for helpful discussions on the phase boundaries and non-equilibrium dynamics. We acknowledge funding from National Key R&D Program of China (2017YFA0304800), NSFC funding (Grant Nos. U20A20218, 61525504, 61722510, 61435011), the Youth Innovation Promotion Association of CAS Grant No. 2018490, EPSRC through grant agreements EP/M014398/1, EP/R002061/1, EP/L023024/1, EP/P012000/1, EP/R035482/1, EP/S015973/1, as well as, DSTL, and Durham University. The European Union’s Horizon 2020 Research and Innovation Program under Grant No. 845218 (Marie Curie Fellowship to H. B.). F.N. was supported in part by NTT Research, JSPS

Grant No. JP20H00134, ARO Grant No. W911NF-18-1-0358, AOARD Grant No. FA2386-20-1-4069, and FQXi Grant No. FQXi-IAF19-06.

* dds@ustc.edu.cn

† drshi@ustc.edu.cn

‡ c.s.adams@durham.ac.uk

§ fnori@riken.jp

- [1] H. Haken, *Information and self-organization: A macroscopic approach to complex systems* (Springer Science & Business Media, 2006).
- [2] P. Bak, C. Tang, K. Wiesenfeld, Self-organized criticality: and explanation of $1/f$ noise. *Phys. Rev. Lett.* **59**, 381–384 (1987).
- [3] S. Field, J. Witt, F. Nori, X. Ling, Superconducting vortex avalanches. *Phys. Rev. Lett.* **74**, 1206 (1995).
- [4] C. Olson, C. Reichhardt, F. Nori, Superconducting vortex avalanches, voltage bursts, and vortex plastic flow. *Phys. Rev. B.* **56**, 6175 (1997).
- [5] P. Schauß, *et al.*, Observation of spatially ordered structures in a two-dimensional Rydberg gas. *Nature* **491**, 87–91 (2012).
- [6] H. Labuhn, *et al.*, Tunable two-dimensional arrays of single Rydberg atoms for realizing quantum Ising models. *Nature* **534**, 667–684 (2016).
- [7] H. Bernien, *et al.*, Probing many-body dynamics on a 51-atom quantum simulator. *Nature* **551**, 579–584 (2017).
- [8] S. de Léséleuc, *et al.*, Observation of a symmetry-protected topological phase of interacting bosons with Rydberg atoms. *Science* **365**, 775–780 (2019).
- [9] D. Bluvstein, *et al.*, Controlling quantum many-body dynamics in driven Rydberg atom arrays. *Science* **371**, 1355–1359 (2021).
- [10] J. Eisert, M. Friesdorf, C. Gogolin, Quantum many-body systems out of equilibrium. *Nature Physics* **11**, 124–130 (2015).
- [11] A. Browaeys, T. Lahaye, Many-body physics with individually controlled Rydberg atoms. *Nature Physics* **16**, 132–142 (2020).
- [12] M. Saffman, T. Walker, K. Mølmer, Quantum information with Rydberg atoms. *Reviews of Modern Physics* **82**, 2313 (2010).
- [13] C. S. Adams, J. D. Pritchard, J. P. Shaffer, Rydberg atom quantum technologies. *Journal of Physics B* **53**, 012002 (2019).
- [14] M. Morgado, S. Whitlock, Quantum simulation and computing with Rydberg-interacting qubits. *AVS Quantum Sci* **3**, 023501 (2021).
- [15] I. Bloch, J. Dalibard, S. Nascimbene, Quantum simulations with ultracold quantum gases. *Nature Physics* **8**, 267–276 (2012).
- [16] I. M. Georgescu, S. Ashhab, F. Nori, Quantum simulation. *Reviews of Modern Physics* **86**, 153 (2014).
- [17] T. F. Gallagher, *Rydberg atoms*, vol. 3 (Cambridge University Press, 2005).
- [18] O. Firstenberg, C. S. Adams, S. Hofferberth, Nonlinear quantum optics mediated by Rydberg interactions. *Journal of Physics B* **49**, 152003 (2016).
- [19] A. Urvoy, *et al.*, Strongly correlated growth of Rydberg aggregates in a vapor cell. *Phys. Rev. Lett.* **114**, 203002

- (2015).
- [20] C. Carr, R. Ritter, C. Wade, C. S. Adams, K. J. Weatherill, Nonequilibrium phase transition in a dilute Rydberg ensemble. *Phys. Rev. Lett.* **111**, 113901 (2013).
- [21] N. Malossi, *et al.*, Full counting statistics and phase diagram of a dissipative Rydberg gas. *Phys. Rev. Lett.* **113**, 023006 (2014).
- [22] M. Marcuzzi, E. Levi, S. Diehl, J. P. Garrahan, I. Lesanovsky, Universal nonequilibrium properties of dissipative Rydberg gases. *Phys. Rev. Lett.* **113**, 210401 (2014).
- [23] S. Helmrich, *et al.*, Signatures of self-organized criticality in an ultracold atomic gas. *Nature* **577**, 481–486 (2020).
- [24] D.-S. Ding, H. Busche, B.-S. Shi, G.-C. Guo, C. S. Adams, Phase diagram and self-organizing dynamics in a thermal ensemble of strongly interacting Rydberg atoms. *Phys. Rev. X* **10**, 021023 (2020).
- [25] T. Wintermantel, *et al.*, Epidemic growth and Griffiths effects on an emergent network of excited atoms. *Nature Communications* **12**, 1–6 (2021).
- [26] K. Klocke, T. Wintermantel, G. Lochead, S. Whitlock, M. Buchhold, Hydrodynamic stabilization of self-organized criticality in a driven Rydberg gas. *Phys. Rev. Lett.* **126**, 123401 (2021).
- [27] S. Eubank, *et al.*, Modelling disease outbreaks in realistic urban social networks. *Nature* **429**, 180–184 (2004).
- [28] I. M. Longini, *et al.*, Containing pandemic influenza at the source. *Science* **309**, 1083–1087 (2005).
- [29] R. Pastor-Satorras, C. Castellano, P. Van Mieghem, A. Vespignani, Epidemic processes in complex networks. *Reviews of modern physics* **87**, 925 (2015).
- [30] Supplementary materials, including experimental setup, optical multistability, theoretical analysis and fast and slow scan effect.
- [31] B. Drossel, F. Schwabl, Self-organized critical forest-fire model. *Phys. Rev. Lett.* **69**, 1629 (1992).
- [32] M. Kitano, T. Yabuzaki, T. Ogawa, Optical tristability. *Phys. Rev. Lett.* **46**, 926 (1981).
- [33] S. Cecchi, G. Giusfredi, E. Petriella, P. Salieri, Observation of optical tristability in sodium vapors. *Phys. Rev. Lett.* **49**, 1928 (1982).
- [34] A. Joshi, M. Xiao, Optical multistability in three-level atoms inside an optical ring cavity. *Phys. Rev. Lett.* **91**, 143904 (2003).
- [35] J. Sheng, U. Khadka, M. Xiao, Realization of all-optical multistate switching in an atomic coherent medium. *Phys. Rev. Lett.* **109**, 223906 (2012).
- [36] N. Gippius, *et al.*, Polarization multistability of cavity polaritons. *Phys. Rev. Lett.* **98**, 236401 (2007).
- [37] T. Paraíso, M. Wouters, Y. Léger, F. Morier-Genoud, B. Deveaud-Plédran, Multistability of a coherent spin ensemble in a semiconductor microcavity. *Nature Materials* **9**, 655–660 (2010).
- [38] D. Sarkar, *et al.*, Polarization bistability and resultant spin rings in semiconductor microcavities. *Phys. Rev. Lett.* **105**, 216402 (2010).
- [39] R. Cerna, *et al.*, Ultrafast tristable spin memory of a coherent polariton gas. *Nature Communications* **4**, 2008 (2013).
- [40] V. Goblot, *et al.*, Nonlinear polariton fluids in a flatband reveal discrete gap solitons. *Phys. Rev. Lett.* **123**, 113901 (2019).
- [41] T. E. Lee, H. Haefner, M. Cross, Collective quantum jumps of Rydberg atoms. *Phys. Rev. Lett.* **108**, 023602 (2012).
- [42] H. Weimer, Variational principle for steady states of dissipative quantum many-body systems. *Phys. Rev. Lett.* **114**, 040402 (2015).
- [43] N. Šibalić, C. G. Wade, C. S. Adams, K. J. Weatherill, T. Pohl, Driven-dissipative many-body systems with mixed power-law interactions: Bistabilities and temperature-driven nonequilibrium phase transitions. *Phys. Rev. A* **94**, 011401 (2016).
- [44] E. Levi, R. Gutiérrez, I. Lesanovsky, Quantum non-equilibrium dynamics of Rydberg gases in the presence of dephasing noise of different strengths. *Journal of Physics B* **49**, 184003 (2016).
- [45] N. R. de Melo, *et al.*, Intrinsic optical bistability in a strongly driven Rydberg ensemble. *Phys. Rev. A* **93**, 063863 (2016).
- [46] D. Weller, A. Urvoy, A. Rico, R. Löw, H. Kübler, Charge-induced optical bistability in thermal Rydberg vapor. *Phys. Rev. A* **94**, 063820 (2016).

**Supplementary materials for: Epidemic spreading and
herd immunity in a driven non-equilibrium system
of strongly-interacting atoms**

Dong-Sheng Ding,^{1,2,*} Zong-Kai Liu,^{1,2} Hannes Busche,³ Bao-Sen
Shi,^{1,2,†} Guang-Can Guo,^{1,2} Charles S. Adams,^{4,‡} and Franco Nori^{5,6,7,§}

¹*Key Laboratory of Quantum Information,
University of Science and Technology of China, Hefei, Anhui 230026, China.*
²*Synergetic Innovation Center of Quantum Information and Quantum Physics,
University of Science and Technology of China, Hefei, Anhui 230026, China.*

³*Department of Physics, Chemistry and Pharmacy, Physics@SDU,
University of Southern Denmark, 5230 Odense M, Denmark*

⁴*Department of Physics, Joint Quantum Centre (JQC) Durham-Newcastle,
Durham University, South Road, Durham DH1 3LE, United Kingdom*

⁵*Theoretical Quantum Physics Laboratory,
RIKEN Cluster for Pioneering Research,
Wako-shi, Saitama 351-0198, Japan.*

⁶*RIKEN Center for Quantum Computing (RQC),
Wako-shi, Saitama 351-0198, Japan.*

⁷*Physics Department, The University of Michigan, Ann Arbor, MI 48109-1040, USA.*

(Dated: June 24, 2021)

* dds@ustc.edu.cn

† drshi@ustc.edu.cn

‡ c.s.adams@durham.ac.uk

§ fnori@riken.jp

I. Experimental setup

The energy diagram and experimental set-up are schematically shown in Fig. S1(a) and (b), respectively. Aside from the addition of the perturbing field, the setup is similar to the one in Ref. [1]. Three atomic levels, a ground state $|g\rangle$, a low-lying excited state $|e\rangle$, and a Rydberg state $|r\rangle$, are driven by a probe (near-resonant with $|g\rangle \rightarrow |e\rangle$) and a coupling field (near-resonant with $|e\rangle \rightarrow |r\rangle$). These fields counter-propagate through a 5 cm long vapour cell filled with ^{85}Rb atoms at $T = 60^\circ\text{C}$. The two lasers excite Rydberg atoms in a ladder-type electromagnetically induced transparency (EIT) configuration [2]. The ground state atom density is $3.3 \times 10^{11} \text{ cm}^{-3}$, corresponding to a mean interatomic spacing of $0.8 \mu\text{m}$. The probe beam is focused into the cell ($1/e^2$ -waist radius $\sim 500 \mu\text{m}$) and couples the ground state $|g\rangle = |5S_{1/2}, F = 3\rangle$ to $|e\rangle = |5P_{1/2}, F' = 2\rangle$ with detuning Δ_p and Rabi frequency Ω_p . The coupling beam ($1/e^2$ -waist radius of $\sim 200 \mu\text{m}$) with detuning Δ_c is resonant with the transition from $|e\rangle$ to a Rydberg state $|r\rangle = |47D_{3/2}\rangle$ with Rabi frequency $\Omega_c \sim 2\pi \times 20 \text{ MHz}$. By using a counter-propagating geometry, the Doppler effect is reduced by a factor of $v(\omega_p - \omega_c)/c$, where v is an atom's velocity, and ω_p and ω_c denote the angular frequencies of the probe and coupling light. If the lifetime of $|r\rangle$ is long compared to $|e\rangle$, (i.e. the decay rates satisfy $\Gamma_r \ll \Gamma_e$, as typically the case for Rydberg states) and the probe is weak compared to the coupling field $\Omega_p \ll \Omega_c$, this corresponds to an EIT configuration where the presence of the resonant coupling field renders the ensemble transparent for the resonant probe light. In the experiment, we fix $\Delta_p = 0$ and observe the transmission as Δ_c is scanned at different rates. The transmission of a reference field (sent through the cell in parallel and not overlapping with the coupling light) is subtracted via a pair of balanced amplified photodiodes. The photoelectric signal of the transmission difference between probe and reference is recorded by a computer.

The additional perturbation schematically shown in Fig. S1(b) represents either one or two perturbing fields, which are of the same type as the probe beam. The Rabi frequencies and angles of these perturbing fields could be tuned individually, to create a spatially inhomogeneous Rydberg excitation rate. In addition, the perturbing fields are coupled to the coupling field in order to satisfy the EIT configuration. They only modulate the Rydberg populations along the path of the probe field, but are not collected by the balanced amplified photodiodes. In this case, the non-equilibrium dynamics of the localized system along the path of the probe field is strongly affected by the perturbation.

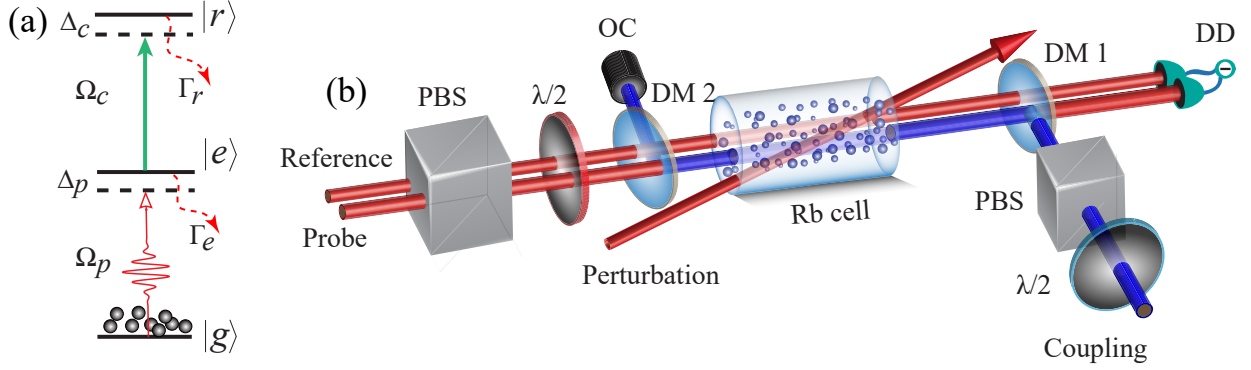


Figure S1. (a) Energy diagram used to excite Rydberg atoms via a two-photon transition using probe and coupling fields with Rabi frequencies, Ω_p and Ω_c , respectively. (b) Overview of the experimental setup. The probe (and an identical reference beam resonant with the $|g\rangle = |5S_{1/2}, F = 3\rangle \rightarrow |e\rangle = |5P_{1/2}, F' = 2\rangle$ transition in ^{85}Rb) propagate in parallel through a heated Rb cell. The coupling light (blue), tuned close to resonance with the $|e\rangle \rightarrow |r\rangle = |47D_{3/2}\rangle$ transition, counter-propagates along the axis of the probe. Additional perturbing fields, with Rabi frequencies Ω_{pert} , are applied at an angle θ . The probe and reference transmission are detected on a differencing photodetector (DD). PBS: polarizing beam splitter, DM: dichroic mirror, $\lambda/2$: half-wave plate, DD: differencing photodetector, OC: optical collector.

II. Optical multistability

A dynamical phase transition can be observed as a jump in the probe transmission as the critical Rydberg density [corresponding to the critical population ρ_{th} , shown as a horizontal red line in Fig. S2(b)] is exceeded, and an optical bistability window can be observed depending on the scan direction and rate of change of Δ_c . The areas beyond the threshold ρ_{th} are marked in red in Fig. S2 (b). To demonstrate how spatial domains—with different excitation dynamics—result in optical multistability, we expose part of the excitation volume to an additional probe light in the form of a single perturbing beam that intersects the probe and control beams at an angle θ , and locally enhances the Rydberg population in the region labelled A in Fig. S1(a), also marked as A in Fig. S1(b). A second local maximum labelled B in Fig. S1(a) occurs at the focus of the probe.

The amplitude of the perturbing field is characterized by a Rabi frequency Ω_{pert} , which can be varied independently of Ω_p . Varying Ω_{pert} can adjust the relative intensity and hence the Rydberg density in regions A and B. As the two domains are characterized by distinct Rydberg populations, they can exhibit either independent or coupled non-equilibrium dynamics depending on the size of the separation region labelled C in Fig. S2. Note that a domain boundary can also arise from attenuating the probe light along the medium [3]. The dynamics of the optical multistability along the z -axis is thus affected by the overall inhomogeneity of the Rydberg density. For any spatially varying intensity distribution, we expect distinct phases that are characterized by a spatial boundary between states of high and low population [4]. In addition to the control offered via Ω_{pert} , we can also vary both the total intensity in region A and its overlap with region B via the alignment of the perturbing beam. As expected, we find that both the intensity in region A and the separation to region B, i.e. C in Fig. S2 are critical. Additional perturbing fields would create more domains.

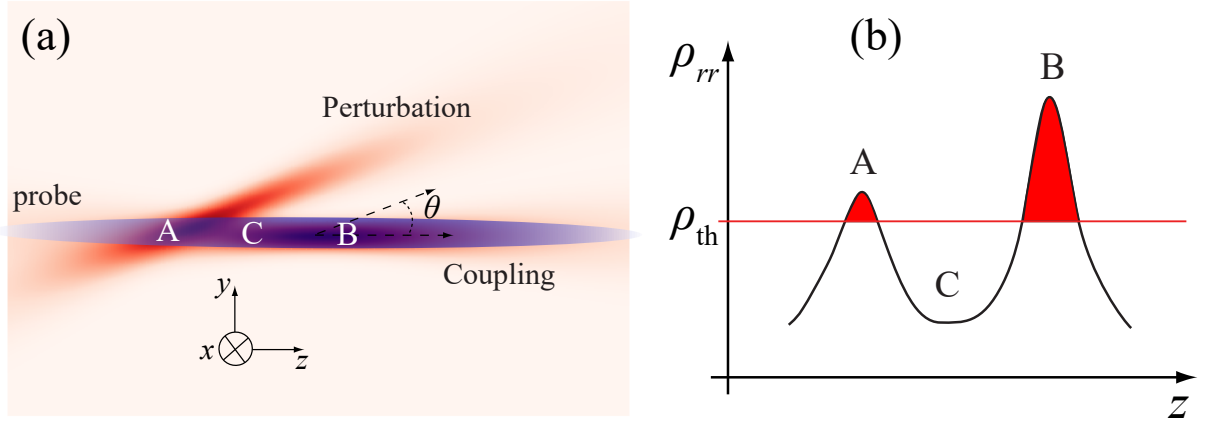


Figure S2. (a) Schematic diagram illustrating the intensity distribution inside the cell. The perturbing beam and focused probe form two distinct high intensity regions labelled A and B, respectively. The relative Rydberg populations in A and B can be controlled by varying Ω_{pert} . (b) Schematic illustration of the Rydberg atom density ρ_{rr} along the optical axis z -coordinate. When $\rho_{rr} > \rho_{\text{th}}$, the critical Rydberg density, a phase transition between a non-interacting and the interacting phase occurs. In region C, between the two domains A and B, the Rydberg density is below threshold.

III. Theoretical analysis

Here we show that the experimental results can be modeled using mean-field optical Bloch equations and qualitatively using an epidemic model. The Lindblad master equation is given by

$$d\rho/dt = -i[H, \rho]/\hbar + L/\hbar, \quad (1)$$

where ρ is the atomic ensemble's density matrix and $H = \sum_k H[\rho^{(k)}]$ the atom-light interaction Hamiltonian summed over all the single-atom Hamiltonians using the rotating wave approximation. The single-atom Hamiltonian has the form:

$$H[\rho^{(k)}] = -\frac{\hbar}{2} \begin{pmatrix} 0 & \Omega_p & 0 \\ \Omega_p & -2\Delta_p & \Omega_c \\ 0 & \Omega_c & -2(\Delta_p - \Delta_c) \end{pmatrix} \quad (2)$$

The Lindblad superoperator $L = \sum_k L[\rho^{(k)}]$ is comprised of the single-atom superoperators, where $L[\rho^{(k)}]/\hbar = -\frac{1}{2} \sum_m (C_m^\dagger C_m \rho + \rho C_m^\dagger C_m) + \sum_m C_m \rho C_m^\dagger$, $C_1 = \sqrt{\Gamma_e} |g\rangle \langle e|$, and $C_2 = \sqrt{\Gamma_r} |e\rangle \langle r|$ are collapse operators for the decay from state $|e\rangle$ to $|g\rangle$ and from $|r\rangle$ to $|e\rangle$ with rates Γ_e and Γ_r , respectively. The matrix form of the Lindbladian can be written as

$$\frac{L[\rho^{(k)}]}{\hbar} = \frac{1}{2} \begin{pmatrix} 2\Gamma_e \rho_{ee}^{(k)} & -\Gamma_e \rho_{ge}^{(k)} & -\Gamma_r \rho_{gr}^{(k)} \\ -\Gamma_e \rho_{eg}^{(k)} & -2\Gamma_e \rho_{ee}^{(k)} + 2\Gamma_r \rho_{rr}^{(k)} & -(\Gamma_e + \Gamma_r) \rho_{er}^{(k)} \\ -\Gamma_r \rho_{rg}^{(k)} & -(\Gamma_e + \Gamma_r) \rho_{re}^{(k)} & -2\Gamma_r \rho_{rr}^{(k)} \end{pmatrix} \quad (3)$$

Since we are only concerned with the steady state, i.e. $t \rightarrow \infty$, the Lindblad master equation can be solved for $d\rho/dt = 0$. The complex susceptibility of the EIT medium including the Doppler effect due to atomic motion is

$$\chi(v)dv = (|\mu_{ge}|^2/\epsilon_0 \hbar) \rho_{eg}(v)dv, \quad (4)$$

the coherence ρ_{eg} in the density matrix is obtained by solving the master equation. It has the form

$$\rho_{eg}(v) = \frac{N(v)[\Gamma_r + 2i(\delta + \Delta_D)]}{(2\Delta_p + 2\omega_p v/c - i\Gamma_e)[\Gamma_r + 2i(\delta + \Delta_D) - i\Omega_c^2]}. \quad (5)$$

where $\Delta_D = (\omega_p - \omega_c)v/c$ denotes the Doppler shift experienced by an atom moving with velocity v , $\delta = \Delta_c + \Delta_p$ is the two-photon detuning, and $N(v)$ is the effective atom number. The spectra of the EIT medium are obtained from the susceptibility via

$$T(\Delta_c, \Gamma_r) \sim \exp\{-\text{Im}[\int kL\chi(v)dv]\}. \quad (6)$$

where L is the medium length and k the wavevector of the probe field. In the Doppler integration, we consider atomic velocities from $v = -500$ m/s to 500 m/s in order to reduce computational complexity. Due to the two spatial domains A and B illustrated in the inset of Fig. S2(b), we assume that there are three distinct steady states, 1, 2, and 3, corresponding to: no domains above threshold; one domain above threshold; and two domains above threshold, respectively. The steady-state lineshapes associated with these three steady-states are plotted as dashed lines in Fig. S3. To calculate these steady-state lineshapes, we assume that both the energy and the decay rate, Γ_r , of the Rydberg state are modified by motional averaging of interaction potentials and Stark shifts Δ_{shift} (due to electric fields created by ions) [3, 5]. These effects are described by

$$\Delta_c \rightarrow \Delta_c + \eta_1 \cdot (f_R - f_{R,c}), \quad (7)$$

and

$$\Gamma_r \rightarrow \Gamma_r + \eta_2 \cdot (f_R - f_{R,c}), \quad (8)$$

when $f_R > f_{R,c}$, where f_R is the fraction of Rydberg atoms, and we set the critical Rydberg fraction, $f_{R,c} = 0.09$, $\eta_1 = 3$ MHz and $\eta_2 = 50$ MHz to match the experimental results. The observation that the broadening exceeds the line shift ($\eta_2 > \eta_1$) is consistent with previous work on Rydberg-induced bistability [1, 5].

When Δ_c is scanned from red- to blue-detuning (positive + scan direction, red line), the transmission initially evolves along the normal EIT resonance curve (steady state 1). As Δ_c approaches resonance, ρ_{rr} increases and eventually one domain (either A or B depending on Ω_{pert}) reaches the threshold ρ_{th} , this threshold effect is also simulated by the epidemic model in the main text. At this detuning [label g in Fig. S3(a)], the system undergoes a non-equilibrium phase transition accompanied by a sudden jump in its optical transmission. Note that the critical detuning also depends on temperature and Ω_p . Increasing Δ_c further, the system initially follows the steady-state 2 resonance curve, and then undergoes a second phase transition at point i in Fig. S3(a) as ρ_{rr} lies above threshold in both domains. In this example, the transition points g and i do not coincide due to different local conditions in the domains A and B. By changing Ω_{pert} , g and i can be moved to coincide. Scanning Δ_c from blue- to red-detuning ($-$ scan direction, black line), the phase transitions occur at points d and b , giving rise to two hysteresis loops, see Fig. S3(a). Depending on system parameters,

the two bistability loops may be either closed [Fig. S3(a)] or open. Three states with different Rydberg fractions, (for example $f_R < 0.9$, $f_R = 0.23$, and $f_R = 0.33$, respectively), are used in the simulations. The system transmission states $T(f_R)$ are treated as EIT transmission with different energy shifts and broadening, given by the gray lines in Fig. S3(a). The multiple discrete transmission levels arise as the transition threshold is reached for different detunings in each domain.

To highlight how the subtle difference in Rydberg population between domains A, B, and C results in optical multistability, we analyze three situations: no-, single- and double-bistability. The spatial variation of the perturbing, probe, and coupling fields leads to a spatially inhomogeneous coupling to the Rydberg state and creates an inhomogeneous Rydberg density. Once the critical Rydberg population in a given region exceeds the threshold population ρ_{th} , the state of the region would transition from the NI to the I phase, and accompanied by a jump in the probe transmission. If the Rydberg population does not exceed the threshold population ρ_{th} in any domain, we only observe a standard EIT spectrum without any jump, as in the case in Fig. S3(b). The probe transmission spectra with + and - scan directions are smooth without sudden change. If the Rydberg population in, e.g. region B, is above ρ_{th} , optical bistability occurs as in the case in Fig. S3(c). We only observe a single bistability because there is only one domain. If the Rydberg population of both domains A and B exceed ρ_{th} , but with different densities, we could observe optical multistability in the spectra, in which the two bistabilities are staggered, as shown in Fig. S3(d).

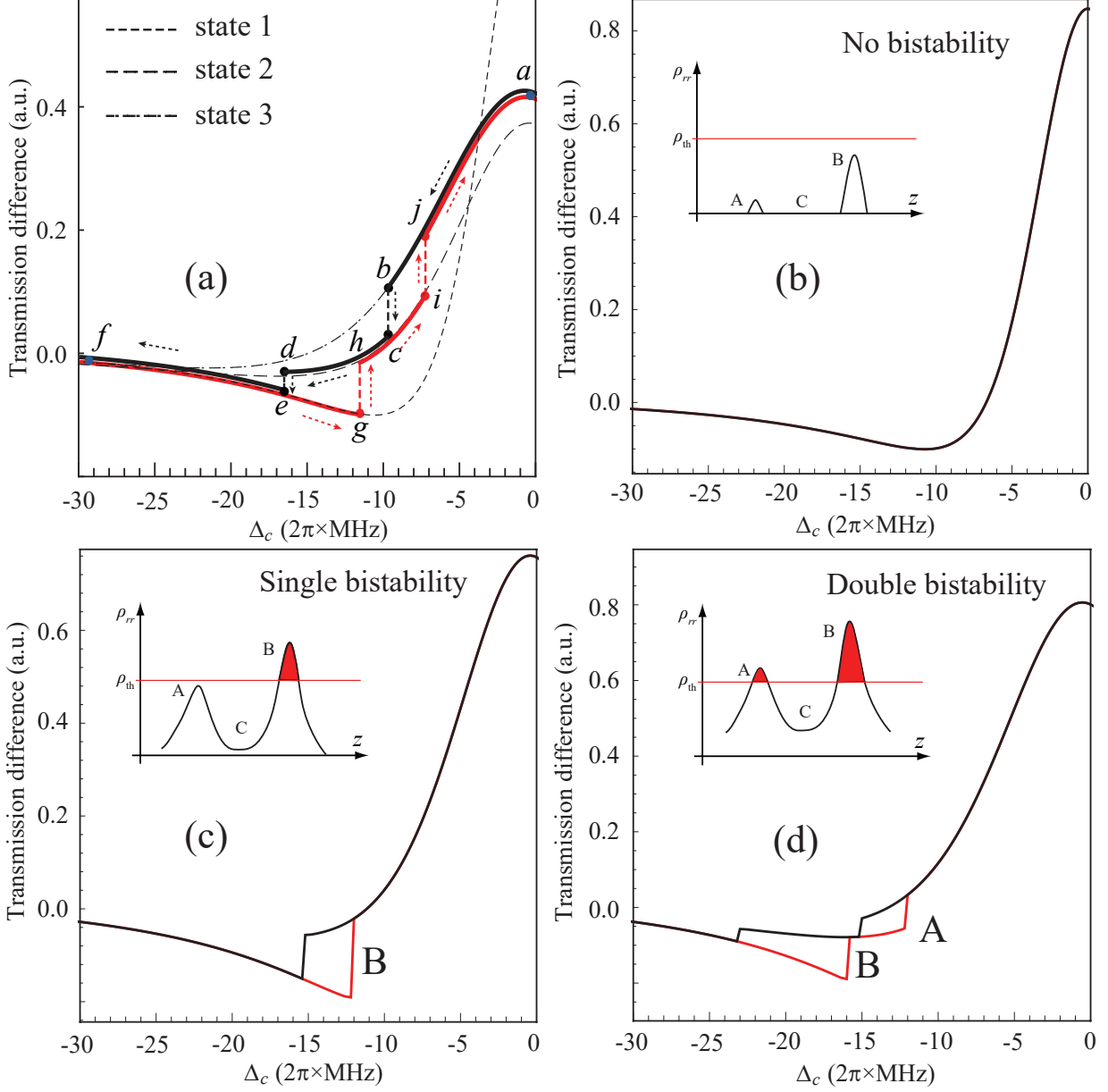


Figure S3. (a) Simplified theoretical simulation of multi-domain bistability. The gray dotted lines correspond to steady states 1, 2 and 3, respectively. The red and black lines are the trajectories when scanning from red- to blue-detuning (red) and vice versa (black). State 1 has a normal EIT transmission with $T(0 < f_R < 0.09)$. State 2 shows the integrated transmission $T(f_R = 0.23)$. State 3 corresponds to $T(f_R = 0.33)$. (b-d) Three cases are compared for (b) no, (c) single bistability in region B only and (d) double bistability in regions A and B. The inserted subfigures describe the Rydberg population under three situations: (b) both of regions A and B are below ρ_{th} ; (c) Region A is below and B is above ρ_{th} ; (d) both of regions A and B are above ρ_{th} .

IV. Comparing experimental and theoretical data for the spatial domains

In order to simulate the behavior of the spatial domains in the phenomenological model, we assign distinct fractions f_{R1} and f_{R2} to each domain and combine their overall optical response. In both theory and experiments, we observe two bistable regimes, and a multi-stable regime where the former coincide. For $\Omega_{\text{pert}} = 2\pi \times 2.4$ MHz [Fig. S4(a1)], we observe similar behaviour predicted in Fig. S1(c) with thresholds (+ scan directions) for state 2 at $\Delta_c \sim -2\pi \times 16$ MHz (transition in domain B) and state 3 at $\Delta_c \sim -2\pi \times 10$ MHz (domain A). To demonstrate control of the phase transition point in domain A, we vary Ω_{pert} from $2\pi \times 2.4$ to $2\pi \times 3.9$ MHz. Scanning Δ_c in either direction, we obtain the experimental spectra shown in Figs. S4(a1-a5). For $\Omega_{\text{pert}} = 2\pi \times 2.4$ MHz, Fig. S4(a1), the hysteresis loops hardly overlap. For $\Omega_{\text{pert}} = 2\pi \times 3.2$ MHz, Fig. S4(a3), the transition appears at the same critical detuning as the phase transitions occur simultaneously in both domains. Comparing Fig. S4(a1-a5) and (b1-b5), the model and experimental data are in good qualitative agreement. But if we choose f_{R1} and f_{R2} to reproduce the experimental thresholds for the + scan direction of Δ_c , we observe slight deviations between the theoretically predicted and experimentally observed thresholds for the - scan direction. If we scan Δ_c more slowly for the parameters in Fig. S4a3, the double bistability appears again because of slight population differences between domains due to fluctuations of the driving fields or vapor temperature.

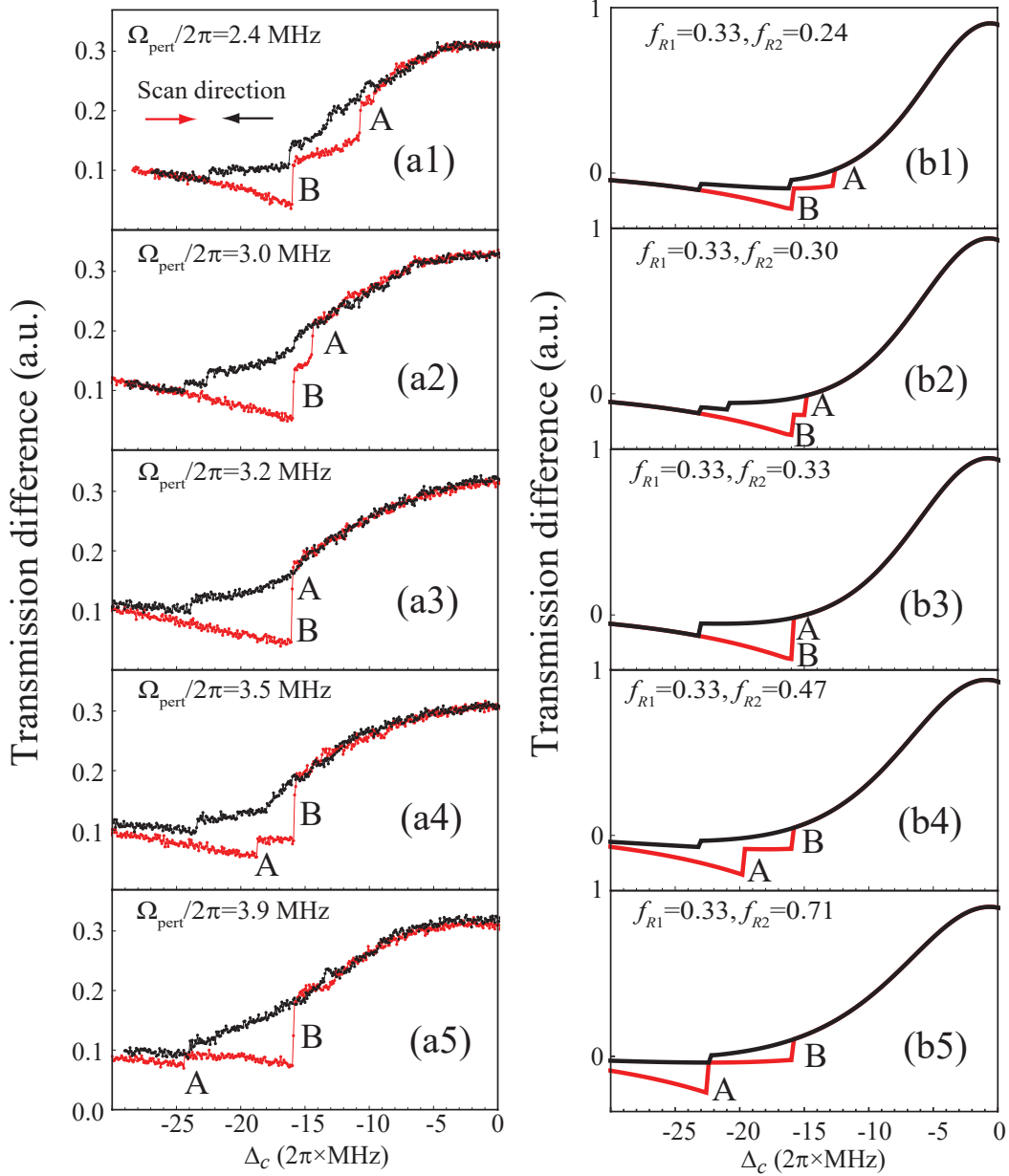


Figure S4. Effect of changing the perturbing field Rabi frequency Ω_{pert} on multi-domain bistability. Comparison of the theoretically (a1-a5) and experimentally (b1-b5) observed probe transmission. Positive (+) and negative (-) scan directions are shown in red and black, respectively. The hysteresis loops for $\Omega_{\text{pert}} = (2\pi \times 2.4, 3.0, 3.2, 3.5, 3.9)$ MHz are shown in Figs. 3(a1-a5), respectively. The phase transitions associated with domains A and B for the + scans are labelled accordingly. Figures b1-b5 show simulations based on our multi-domain model. In the model, we use the Rydberg fractions $f_{R1} = 0.33$ and $f_{R2} = 0.24$ (b1), $f_{R2} = 0.30$ (b2), $f_{R2} = 0.33$ (b3), $f_{R2} = 0.47$ (b4), $f_{R2} = 0.71$ (b5), where f_{Rj} are the fractions of Rydberg atoms in the interaction volumes A and B, respectively (see text). The Rabi frequency of the probe is set to $\Omega_p = 2\pi \times 5.7$ MHz.

V. Susceptible infected-susceptible and susceptible-infected-recovered models

Two typical epidemic spreadings can be described by the susceptible-infected-susceptible (SIS) and susceptible-infected-recovered (SIR) models, as shown in Fig. S5(a). The SIS model has two simple transitions: (1) $S \rightarrow I$ happening when a susceptible individual S interacts with an infected I and becomes infected; (2) the reverse process $I \rightarrow S$ occurs when the infected individual I becomes susceptible. The SIS model does not have an immunity state, and remains in the permanent cycle $I \rightarrow S \rightarrow I$. The SIR model consists of three states: the susceptible S , infected I , and recovered states R . The main difference between the SIR and SIS models is that $I \rightarrow S$ is replaced by $I \rightarrow R$ in SIR model. The process $I \rightarrow R$ corresponds to the infected individual I recovering to be immune R via isolation and medication.

In order to demonstrate the spatial evolution of the epidemic, we build a cellular automaton iteration algorithm as discussed in the main text. We investigate the dynamical results of the SIS and SIR models as we change the fractions f_R of the susceptible state. We show the spreading dynamics of the infected state after different iterations $i = 2, 20, 40, 60$, for different fractions f_R . For low fractions f_R , e.g. $f_R < 0.2$, there is almost no spread because there are not enough susceptible individuals to match close neighbor contact, while for larger fractions f_R , i.e. $f_R = 0.9$ shown in Fig. S5(b) (SIR model), the infected state is more inclined to spread through all the volume. We also observe the evolution of the SIS model with $f_R = 0.55$: the infected individuals spread along local trajectories and result in a specific graph state [SIR model in Fig. S5(b)].

Eventually, the final states of evolution for these two models are different. For the SIS model, the system follows a stationary state due to the cycle $I \rightarrow S \rightarrow I$; see the evolution of the system after the iteration $i = 60$ [SIS model in Fig. S5(b)]. This stationary effect satisfies the character of “endemic state” in which the dynamic equilibrium between the susceptible and infected state is sustained for a long time. While in the SIR model, due to the recovery channel $S \rightarrow R$, most of the red and green cells change to black cells after multiple iterations [SIR model in Fig. S5(b)], and the system finally reaches an immune state in which all infected individuals are healthy. This describes the process of “herd immunity”.

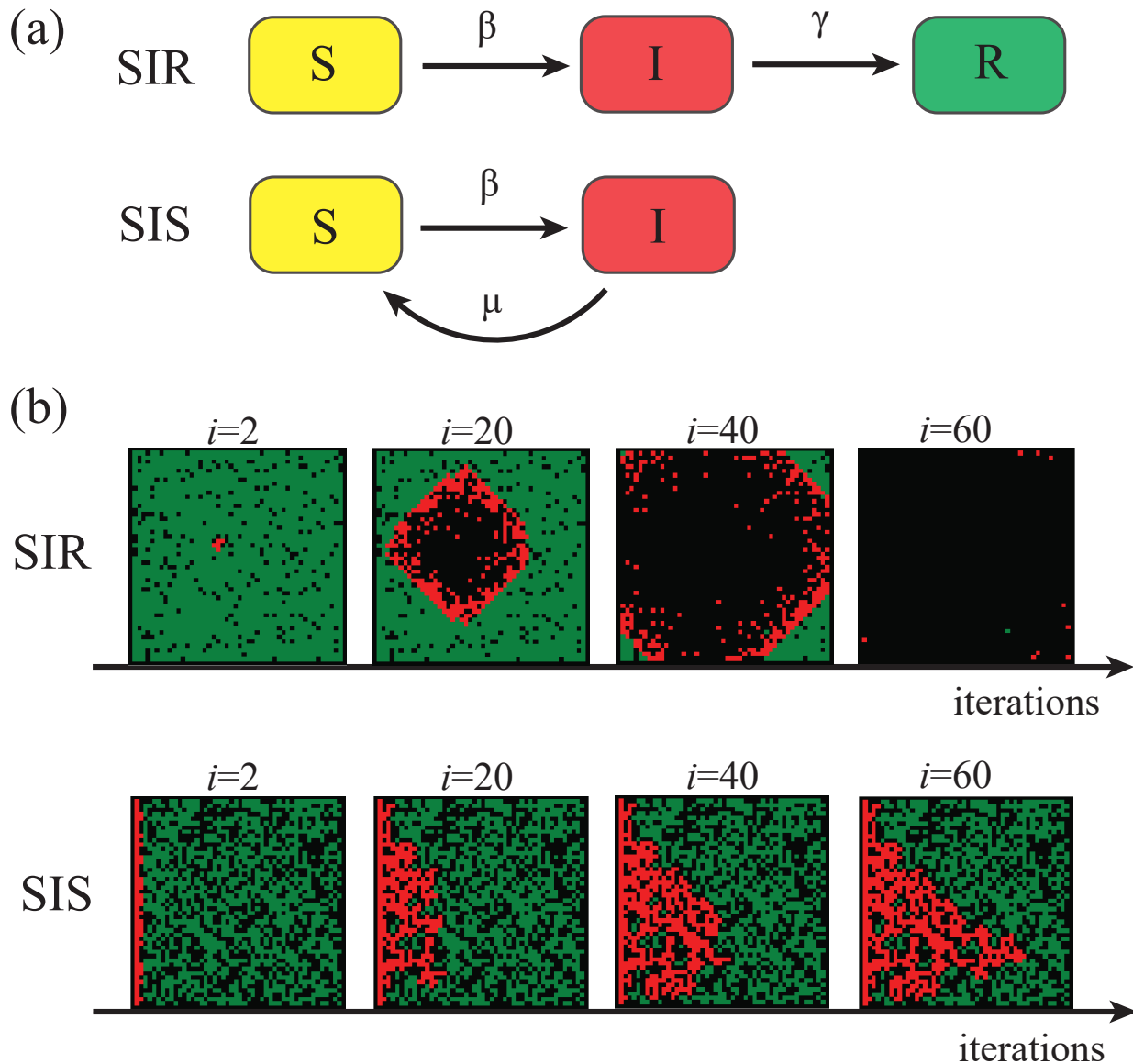


Figure S5. (a) Diagrammatic representation of the SIS and SIR models in terms of reaction-diffusion processes. Boxes represent different disease states, while the arrows represent the stochastic transitions between these states. Note that S: susceptible state; I: infected state; R: recovered state; β represents the probability of the transition $S \rightarrow I$; γ is the recovery probability from infected I to recovered R via isolation and medication; μ is the probability of the transition $I \rightarrow S$, corresponding to when the infected individuals have not been immunized. (b) A 2D snapshot of interacting Rydberg atoms spreading in a 50×50 system after iterations $i = 2, 20, 40, 60$, respectively for $f_R = 0.9$ (SIR model) and $f_R = 0.55$ (SIS model). Red cells correspond to the infected state I , green cells the susceptible state S , and black cells the recovered state R .

VI. Effects of fast and slow scan of the detuning

At a low scan rate of Δ_c , the spreading dynamics of the interacting phase population is affected by the finite lifetime of the Rydberg state, as well as the interacting phase, compared to the sweep speed of the coupling detuning Δ_c [Fig. S6]. The interacting Rydberg population would oscillate between $\Delta_c = 2\pi \times -21.3$ MHz and $\Delta_c = 2\pi \times -20.8$ MHz, which corresponds to the case when $\beta\Delta t \sim \gamma\Delta t$ and $\mu\Delta t \rightarrow 0$ in the relatively longer time interval Δt , see Fig. S6(b). Here, the increase in coupling strength to the Rydberg state arising from the detuning scan is low, and the interacting phase cannot be sustained because the decay plays a role in the interacting phase spreading out. In addition, due to the decay of the interacting Rydberg atoms, and the refilling atoms from the thermal motions, then the system exhibits self-organized quasi-criticality [6], making the system unstable in the interacting phase. Moreover, a phase transition without oscillation appears at a fast scan rate of Δ_c , see Fig. S6(a); in this case, the spreading rate β is larger than the decay rate γ , thus $\gamma\Delta t \rightarrow 0$ or $\beta\Delta t \gg \gamma\Delta t, \mu\Delta t$ in a relatively short time interval Δt .

The system under the different regimes shows a different non-equilibrium dynamics. Our experiments in the fast-scan regime follow the predictions of the SIS model. In the fast-scan, the interacting Rydberg atoms do not have enough time to decay, because the increased Rydberg population would supply the system when scanning Δ_c fast. Although the interacting Rydberg atoms are constantly supplied, there are still some interacting atoms decaying into non-interacting atoms. But in a relatively long time, the system would reach a stationary state, where the interacting and the non-interacting Rydberg atoms are in dynamical equilibrium. This process follows the predictions of the SIS model: the disease does not confer immunity and individuals can be infected over and over again, undergoing a cycle of susceptible state \rightarrow infected state \rightarrow susceptible state, which, under some conditions, can be sustained in a long time [7]. While in slow- or no-scan regime, the system follows the predictions of the SIR model. The system near the critical point would undergo a self-organized phase, where the lost atoms are not effectively replenished, thus the interacting phase would transit to the no-interacting phase. For relatively long times, the interacting Rydberg atoms have enough time to be lost below the threshold ρ_{th} , and this corresponds to the process of infectious individuals recovering from the disease in the SIR model.

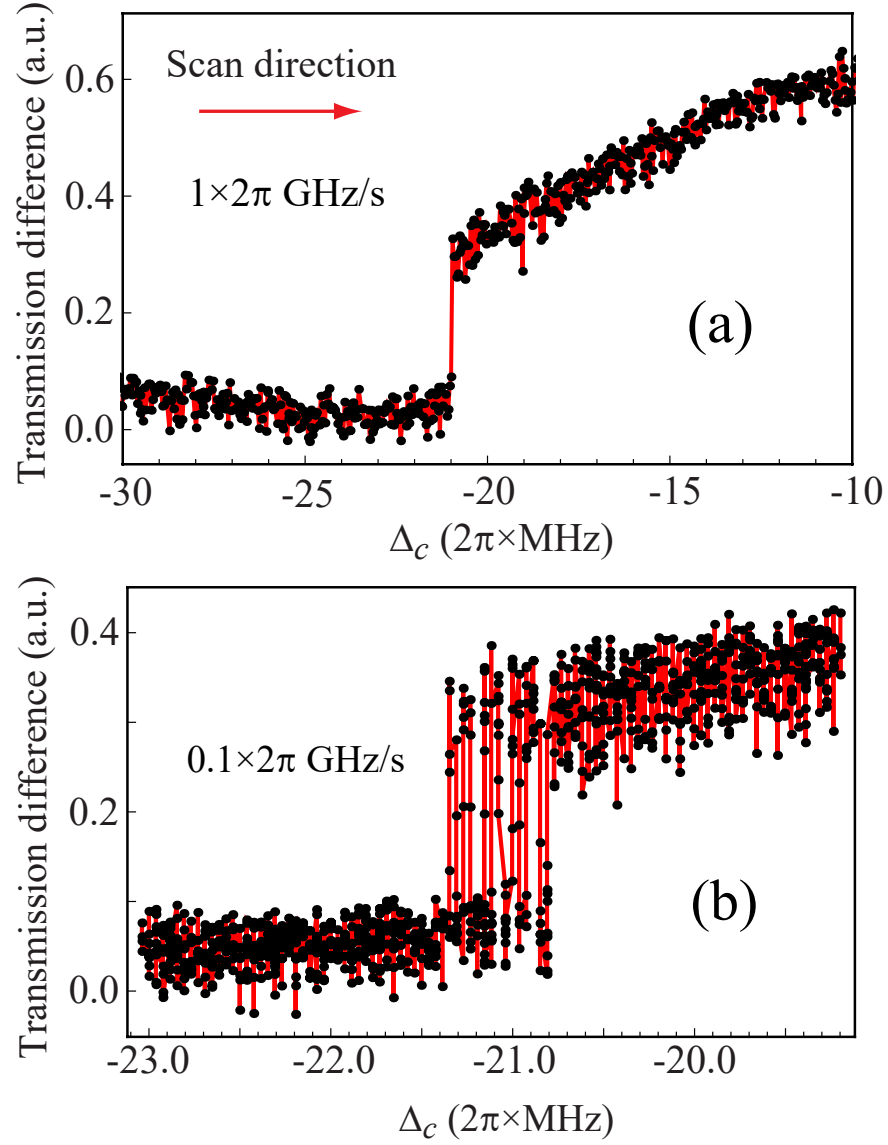


Figure S6. Transmission in the vicinity of the critical threshold for scan rates of $1 \times 2\pi \text{ GHz/s}$ (a) and $0.1 \times 2\pi \text{ GHz/s}$ (b). For slow scans, the Rydberg density can become insufficient to sustain the interacting phase as the decay dominates over the change in coupling strength to the Rydberg state from the scan.

-
- [1] D.-S. Ding, H. Busche, B.-S. Shi, G.-C. Guo, C. S. Adams, Phase diagram of non-equilibrium phase transition in a strongly-interacting Rydberg atom vapour. *Phys. Rev. X* **10**, 021023 (2020).
- [2] A. Mohapatra, T. Jackson, C. Adams, Coherent optical detection of highly excited Rydberg states using electromagnetically induced transparency. *Phys. Rev. Lett.* **98**, 113003 (2007).
- [3] C. Carr, R. Ritter, C. Wade, C. S. Adams, K. J. Weatherill, Nonequilibrium phase transition in a dilute Rydberg ensemble. *Phys. Rev. Lett.* **111**, 113901 (2013).
- [4] R. Inguva, C. M. Bowden, Spatial and temporal evolution of the first-order phase transition in intrinsic optical bistability. *Physical Review A* **41**, 1670 (1990).
- [5] D. Weller, A. Urvoy, A. Rico, R. Löw, H. Kübler, Charge-induced optical bistability in thermal Rydberg vapor. *Phys. Rev. A* **94**, 063820 (2016).
- [6] K. Klocke, T. Wintermantel, G. Lohead, S. Whitlock, M. Buchhold, Hydrodynamic stabilization of self-organized criticality in a driven Rydberg gas. *Phys. Rev. Lett.* **126**, 123401 (2021).
- [7] R. Pastor-Satorras, C. Castellano, P. Van Mieghem, A. Vespignani, Epidemic processes in complex networks. *Reviews of Modern Physics* **87**, 925 (2015).